Publication Year	2015
Acceptance in OA@INAF	2020-04-09T13:17:26Z
Title	A Common Stochastic Process Rules Gamma-ray Burst Prompt Emission and X-ray Flares
Authors	Guidorzi, C.; Dichiara, S.; Frontera, F.; Margutti, R.; Baldeschi, A.; et al.
DOI	10.1088/0004-637X/801/1/57
Handle	http://hdl.handle.net/20.500.12386/23960
Journal	THE ASTROPHYSICAL JOURNAL
Number	801

The Astrophysical Journal, 801:57 (11pp), 2015 March 1 doi:10.1088/0004-637X/801/1/57

© 2015. The American Astronomical Society. All rights reserved.

A COMMON STOCHASTIC PROCESS RULES GAMMA-RAY BURST PROMPT EMISSION AND X-RAY FLARES

C. Guidorzi[1], S. Dichiara[1], F. Frontera[1,2], R. Margutti[3], A. Baldeschi[1], and L. Amati[2]
[1] Department of Physics and Earth Sciences, University of Ferrara, via Saragat 1, I-44122, Ferrara, Italy
[2] INAF-IASF Bologna, via Gobetti 101, I-40129, Bologna, Italy
[3] Harvard-Smithsonian Center for Astrophysics, 60 Garden St., Cambridge, MA 02138, USA.

Received 2014 December 6; accepted 2015 January 11; published 2015 March 4

ABSTRACT

Prompt γ-ray and early X-ray afterglow emissions in gamma-ray bursts (GRBs) are characterized by a bursty behavior and are often interspersed with long quiescent times. There is compelling evidence that X-ray flares are linked to prompt γ-rays. However, the physical mechanism that leads to the complex temporal distribution of γ-ray pulses and X-ray flares is not understood. Here we show that the waiting time distribution (WTD) of pulses and flares exhibits a power-law tail extending over four decades with an index of about two and can be the manifestation of a common time-dependent Poisson process. This result is robust and is obtained on different catalogs. Surprisingly, GRBs with many ($\geqslant 8$) γ-ray pulses are very unlikely to be accompanied by X-ray flares after the end of the prompt emission (3.1σ Gaussian confidence). These results are consistent with a simple interpretation: a hyperaccreting disk breaks up into one or a few groups of fragments, each of which is independently accreted with the same probability per unit time. Prompt γ-rays and late X-ray flares are nothing but different fragments being accreted at the beginning and at the end, respectively, following the very same stochastic process and likely the same mechanism.

Key words: gamma-ray burst: general – methods: statistical

1. INTRODUCTION

The first electromagnetic messenger of a gamma-ray burst (GRB) is the so-called γ-ray prompt emission, followed by the early X-ray afterglow on a timescale from minutes to hours. Long-duration (>2–3 s) GRBs are nowadays known to be associated with the core collapse of some kind of massive stars rid of hydrogen envelopes (see Woosley & Bloom 2006; Hjorth & Bloom 2012 for reviews). Prompt γ-rays (with energies in the kiloelectronvolt to megaelectronvolt range) are observed within a given GRB as a sequence of pulses (typically a few up to several dozens). In addition, for a sizable fraction of GRBs, the subsequent decaying X-ray emission, which marks the end of the γ-rays, is characterized by the presence of X-ray flares that are sometimes observed as late as 10^5 s (Burrows et al. 2005; Chincarini et al. 2007; Falcone et al. 2007; Curran et al. 2008; Bernardini et al. 2011). Although mounting evidence exists that X-ray flares, like γ-ray pulses, result from the GRB inner engine activity rather than from external shocks (Lazzati & Perna 2007; Chincarini et al. 2010; Margutti et al. 2010), key questions remain unanswered: what radiation process(es)? What information on the inner engine can we extract? Is there a common process ruling inner engine activity across several decades in time?

As a matter of fact, both emissions represent a temporal point process, i.e., a time series characterized by the discrete occurrence of impulsive events superposed on a continuum. Intense bursting periods are often interspersed with relatively long (several up to tens of seconds) intervals with very low activity, compatible with the detector background, which are often referred to as quiescent times (QTs; Ramirez-Ruiz & Merloni 2001; Nakar & Piran 2002; Quilligan et al. 2002; Drago & Pagliara 2007). The study of the waiting time distribution (WTD), i.e., of how time intervals between adjacent peaks distribute, provides clues on the nature of the stochastic process. In particular, it reveals the degree of memory and correlation and constrains the physical process responsible for the discontinuous and bursty release of energy.

Processes showing similar on–off intermittency or, equivalently, bursty behavior or clusterization can be found in many fields (Platt et al. 1993). The corresponding WTDs often show power-law tails at long waiting times (WTs), whose index depends on the degree of clusterization of the time series. Examples encompass the aftershock sequence observed in earthquakes, described by Omori's law (Utsu 1961), neuronal firing activity, as well as a wide range of dynamical systems of human activity, such as mail and e-mail exchanges (Eckmann et al. 2004; Oliveira and Barabási 2005), phone calls (Karsai et al. 2012 and references therein), all the way to violent conflicts (Picoli et al. 2014). These processes are often modeled and interpreted in the context of self-organized criticality (SOC), where a nonlinear dynamical system reaches a stable critical point in which continuous energy input is released intermittently through avalanches and in a scale-free way. SOC naturally predicts power laws in energy and WT distributions. See Aschwanden et al. (2014) for a recent review on the many areas displaying SOC behavior.

In astrophysics, WTDs are studied for many different kinds of sources, such as outbursting magnetars (Göğüş et al. 1999, 2000; Gavriil et al. 2004), flare stars (Arzner and Güdel 2004), and particularly the activity of the Sun throughout its cycle. WTDs of solar X-ray flares exhibit power-law tails with indices in the range 2.0–2.4 across several decades (Boffetta et al. 1999; Wheatland 2000), depending on the class of flares and flux thresholds. Related bursty emissions from the Sun such as coronal mass ejections (CMEs) are found to show very similar WTDs, whose index ranges from ~1.9 to ~3.0 in low- to high-activity periods of the solar cycle (Wheatland 2003). Likewise, WTDs of solar radio storms (Eastwood et al. 2010), of solar energetic particles, and of solar electron events show very similar power-law indices (Li et al. 2014). Such WTDs with power-law tails are usually interpreted as the consequence of a time-varying Poisson process produced by SOC systems, in which the energy input rate is intermittent and directly affects the degree of clusterization of flares (Aschwanden & McTiernan 2010; Li et al. 2014). In this model, the bursty energy release is the result of avalanches produced in active regions where the magnetic flux is twisted by the moving footpoints, leading to a series of independent magnetic reconnection events and consequent plasma acceleration. Alternatively to SOC, interpretations in the context of fully developed MHD turbulence have also been proposed to explain the bursty dynamics and the power-law WTD: the intermittent character is the result of a nonlinear dynamics that makes the convective motion of the fluid and magnetic field swing between laminar and turbulent regimes repeatedly and chaotically (Boffetta et al. 1999; Lepreti et al. 2004).

The WTD between adjacent peaks in GRB γ-ray prompt emission profiles was found to be described by a lognormal, which implies some degree of memory (Li & Fenimore 1996), with an excess at long values due to QTs (Nakar & Piran 2002; Quilligan et al. 2002; Drago & Pagliara 2007). However, when the peak detection efficiency is carefully taken into account, it is found that the intrinsic WTD at short values is also compatible with an exponential, as is expected for a *constant* Poisson (and thus memoryless) process (Baldeschi & Guidorzi 2015). On the other side of the distribution, long QTs could either mark the inner engine temporarily switching off, or result from modulation of the relativistic wind of shells (Ramirez-Ruiz et al. 2001), or they could be due to a different physical mechanism from that of short WTs (e.g., Drago et al. 2008).

In spite of the impressive data that are routinely being acquired in the *Swift* era, little progress has been reported on WTDs in GRBs. Recently, energy and WT distributions for GRB X-ray flares have been shown to have power-law tails very similar to what is observed for solar X-ray flares. In particular, the WTD has a power-law index of 1.8 ± 0.2 (Wang & Dai 2013). These results were interpreted as evidence for SOC possibly driven by magnetic reconnection episodes triggered in magnetized shells emitted by differentially rotating millisecond pulsars or, alternatively, by a hyperaccreting disk around a black hole (Popham et al. 1999).

Yet, there are several crucial issues that can be tackled with WTDs. Is there additional evidence for a link between prompt γ-rays and late X-ray flares? To what extent do QTs differ from short WTs? Is it possible to provide a common description of short WTs, QTs, and X-ray flares? What about rest-frame properties? Is there evidence for memory in GRB engines? What can be inferred on GRB engines through the WTD study?

In this paper we address these issues through the analysis of the WTD of GRB prompt peaks for three independent data sets: *Swift*/BAT, *CGRO*/BATSE, and *Fermi*/GBM. For the *Swift* GRBs that have also been promptly observed with the X-ray Telescope (XRT), we present a joint analysis of γ-ray peaks and X-ray flares merged together. Section 2 describes the data sample selection and how we modeled the WTDs. Here we deliberately did not consider the energy distribution of peaks and flares because even though our peak search algorithm identified moderately overlapped pulses, estimating their energy would require specific assumptions on their temporal structure. We therefore decided to postpone it for future investigation. The results and their implications and interpretation are reported in Sections 3 and 4, respectively. Hereafter, uncertainties on best-fit parameters are given at 90% confidence, unless stated otherwise.

2. DATA ANALYSIS

We searched all long-duration γ-ray light curves with MEPSA[4] (Guidorzi 2015, 2014), a peak search algorithm designed and calibrated to this goal. The advantage of MEPSA compared with analogous algorithms such as the one by Li & Fenimore (1996) (LF) is twofold:

1. It has a lower false-positive rate. This is particularly true for the time intervals in which the signal drops to background between two adjacent activity periods: in the best cases the LF false-positive rate is $3\text{–}5 \times 10^{-3}$ bin^{-1}, and the MEPSA one is $1\text{–}2 \times 10^{-5}$ bin^{-1} (Guidorzi 2015).
2. It has a higher true-positive rate, especially at low signal-to-noise ratio (S/N) (~4–5).

2.1. Sample Selection

2.1.1. Swift/BAT Data

We started with the GRBs detected by *Swift*/BAT in burst mode from 2005 January to 2014 September, collecting 825 GRBs. We extracted the mask-weighted light curves in the 15–150 keV energy band with a uniform bin time of 64 ms following the standard procedure recommended by the BAT team[5] and applied MEPSA. We then imposed a minimum threshold of 5σ significance, which ensures a very low false-positive rate ($<10^{-5}$ bin^{-1}; Guidorzi 2015) and selected the GRBs with at least two peaks. We then removed from our sample the short-duration GRBs (both with and without extended emission) by cross-checking with the classification provided in the BAT catalog (Sakamoto et al. 2011), as they will be the subject of future investigation. Because this catalog does not include GRBs from 2010, for these GRBs we used the T_{90} values as published in the BAT refined Gamma-ray Coordinate Network (GCN) circulars regularly published by the BAT team and set a conservative minimum threshold of $T_{90} > 3$ s. A couple of GRBs detected by BAT exhibited a very long duration that could not be covered entirely in burst mode: in one case we used the *WIND*/Konus light curve for GRB 091024 (Virgili et al. 2013), and in the case of GRB 130925A we used the peak times as they have been obtained by Evans et al. (2014) from the corresponding Konus light curve. Finally, we ended up with a sample of 418 long GRBs with at least two significant ($>5\sigma$) peaks each, totaling 2,000 peaks and 1,582 WTs. Hereafter, we refer to this sample as the BAT set.

2.1.2. CGRO/BATSE Data

We took the concatenated 64 ms burst data distributed by the BATSE team.[6] For each curve we interpolated the background by fitting with polynomials of up to fourth degree, as suggested by the BATSE team (e.g., Guidorzi 2005). Like in the BAT case, we applied MEPSA to an initial sample of 2,024 light curves in the full passband. We applied the same selection on the peak significance and selected the long GRBs by requiring $T_{90} > 2$ s, where T_{90} was taken from the GRB catalog[7] (Paciesas et al. 1999). We ended up with a sample of 1,089 long GRBs with at least two 5σ significant peaks. Overall we collected 7,649 peaks and 6,560 WTs. Hereafter, this will be referred to as the BATSE sample.

---

[4] http://www.fe.infn.it/u/guidorzi/new_guidorzi_files/code.html

[5] http://swift.gsfc.nasa.gov/analysis/threads/bat_threads.html

[6] ftp://cossc.gsfc.nasa.gov/compton/data/batse/ascii_data/64ms/

We also applied the same selection procedure to the light curves corresponding to the sum of the two softest energy channels (1 and 2) and to the sum of the two hardest channels (3 and 4), respectively, within the 25–110 and >110 keV bands. We collected 1,065 and 922 GRBs, with 5,156 and 4,912 WTs, respectively. These two groups will be hereafter referred to as the BATSE12 and BATSE34 sets, respectively.

2.1.3. Fermi/GBM Data

We selected 586 long GRBs detected with *Fermi*/GBM (Meegan et al. 2009) from 2008 July to 2013 December. We extracted the light curves of the two brightest GBM units in the energy band 8–1000 keV with 64 ms resolution and subtracted the background through interpolation with a polynomial of up to third degree. We selected the long GRBs by imposing $T_{90} > 2$ s, where T_{90} was taken from the official catalog.[8] We restricted it to time intervals whose median values range from −30 to 300 s with reference to the trigger time. This corresponds to the time interval covered by the time-tagged event data type in trigger mode (Paciesas 2012; Gruber et al. 2014). Before −30 s and after 600 s the time resolution is that of the CTIME data, 0.256 s. In most cases we did not consider intervals $t > 300$ s because an interpolation-estimated background often becomes critical and the required effort for a proper estimate is beyond our scope (Gruber et al. 2011; Fitzpatrick et al. 2012). We did not consider GRBs showing prolonged activity beyond this time interval. We then applied the same selection criteria as for the previous sets. Finally, by visual inspection we removed phosphorescence spikes that are due to high-energy particles (Meegan et al. 2009) by comparing the same profiles in different GBM units. We ended up with a final sample of 2,380 peaks out of 544 GRBs with at least two significant peaks. The total number of WTs is 1,839.

2.1.4. Swift/XRT X-Ray Flares

We considered the catalog of 498 X-ray flare candidates detected with *Swift*/XRT obtained by Swenson & Roming (2014). This was extracted from 680 XRT light curves from 2005 January to 2012 December with a method based on the identification of break points in the residuals of the fitted piecewise power-law light curves: these points mark sudden changes in the mean value due to unfitted features. The optimal set of break points was then found by minimizing the residual sum of squares against piecewise constant functions. To counter the effect of overfitting with unnecessary break points, they made use of the Bayesian information criterion (see Swenson et al. 2013; Swenson & Roming 2014 for further details). In this catalog each candidate is assigned a confidence value. We conservatively selected the subsample with a minimum confidence of 90%, ending up with 205 X-ray flare candidates.

We separately merged each X-ray flare catalog with the BAT one by joining, for each GRB, the sequence of γ-ray peak times and flare peak times into a unique sequence of temporal peaks. In doing this, every peak that was seen in both instruments was tagged as a γ-ray peak and not considered any more as an X-ray flare. Analogously to the requirements for the previous sets, we selected those GRBs with at least two (either γ-ray or X-ray) peaks so as to have at least one WT. We ended up with a sample of 1,098 (954 γ-ray and 144 X-ray) peaks in 244 GRBs (2005 January–2012 December). We hereafter refer to this joint set as the BAT-X sample.

Finally, we selected the subsample with known redshift so as to derive the WTD in the source rest frame. This was done by simply correcting for cosmic dilation and thus dividing the observed WTs by the corresponding $(1 + z)$. Unlike the width of a given pulse, which is affected not only by cosmic dilation but also by the energy passband shift, for their nature WTs are affected by the latter to a much lesser extent. We found 359 WTs in 94 GRBs with known redshift. The subset with known redshift will be referred to as BAT-Xz.

As an independent check, we in parallel considered the X-ray flare catalogs of Chincarini et al. (2010) and Bernardini et al. (2011), which respectively include 113 early-time ($t < 10^3$ s) X-ray flares from 2005 April to 2008 March and 36 late-time ($t > 10^3$ s) flares from 2005 April to 2009 December. However, because of lower statistics, we hereafter focus on the BAT-X sample.

2.2. WTD Modeling

In physics, a Poisson process is usually assumed to be characterized by a constant expected rate. The WTD of this process is exponential with e-folding $\tau = 1/\lambda$:

$$P(\Delta t) = \frac{1}{\tau}\, e^{-\Delta t/\tau} = \lambda\, e^{-\lambda\, \Delta t}, \qquad (1)$$

where λ is the constant mean rate and τ is the mean WT. A time-varying Poisson process is characterized by a variable mean rate $\lambda(t)$: the process is locally Poisson, but the expected rate changes with time as described by $\lambda(t)$. According to this definition, the resulting process is the combination of two different processes at play and is often referred to as a "Cox process" (e.g., Cox & Isham 1980):

a. At a given time, t events are generated according to a Poisson process with rate $\lambda = \lambda(t)$ and, as such, are statistically independent
b. The expected rate λ is itself a function of time, which can vary either randomly or deterministically as time passes.

To derive the corresponding WTD, one may approximate $\lambda(t)$ as a piecewise constant function in a number of adjacent time intervals t_i $(i = 1, \ldots, n)$ and treat it as a sequence of several Poisson processes with rate λ_i. Following Aschwanden & McTiernan (2010) and references therein, the resulting WTD is

$$P(\Delta t) \;\approx\; \sum_i \phi\left(\lambda_i\right) \lambda_i\, e^{-\lambda_i\, \Delta t}, \qquad (2)$$

---

[7] http://gammaray.msfc.nasa.gov/batse/grb/catalog/current/tables/duration_table.txt

[8] http://heasarc.gsfc.nasa.gov/W3Browse/fermi/fermigbrst.html

where

$$\phi(\lambda_i) = \frac{\lambda_i\, t_i}{\sum_j \lambda_j t_j}, \tag{3}$$

is proportional to the expected number of WTs in interval t_i where $\lambda = \lambda_i$. In the continuous limit, Equation (2) becomes

$$P(\Delta t) = \frac{\int_0^T \lambda(t)^2\, e^{-\lambda(t)\Delta t} dt}{\int_0^T \lambda(t) dt}, \tag{4}$$

where T is the total duration. When $\lambda(t)$ is either unknown or hard to treat, it is possible to define $f(\lambda)$ such that $f(\lambda)d\lambda = dt/T$, that is, the fraction of time during which the expected rate lies within the range $[\lambda, \lambda + d\lambda]$. Equation (4) becomes

$$P(\Delta t) = \frac{\int_0^{+\infty} f(\lambda)\lambda^2\, e^{-\lambda\,\Delta t} d\lambda}{\int_0^{+\infty} \lambda f(\lambda) d\lambda}. \tag{5}$$

We adopted the model for $f(\lambda)$ provided by Li et al. (2014) in their Equation (5), which has been proposed to fit the WTD obtained for solar X-ray flares and solar energetic particle events:

$$f(\lambda) = A\, \lambda^{-\alpha} \exp(-\beta\, \lambda), \tag{6}$$

with α and β free parameters, and A is a normalization term $(0 \leqslant \alpha < 2)$. This model generalizes several other models that had been put forward in the same context (Wheatland 2000; Aschwanden & McTiernan 2010). The mean rate $\bar{\lambda}$ is

$$\bar{\lambda} = \int_0^{+\infty} \lambda f(\lambda) d\lambda = A\, \beta^{\alpha-2}\, \Gamma(2-\alpha), \tag{7}$$

where $\Gamma()$ is the gamma function. From Equations (5)–(6) the corresponding WTD is

$$P(\Delta t) = (2-\alpha)\beta^{2-\alpha}(\beta + \Delta t)^{-(3-\alpha)}, \tag{8}$$

and it is normalized like a probability density function (PDF), i.e., $\int_0^{+\infty} P(\Delta t) d(\Delta t) = 1$. There are only two free parameters, α, which determines the level of clusterization, and the characteristic WT β at which the WTD breaks: at $\Delta t \gg \beta$, Equation (8) becomes a power law with an index of $(3 - \alpha)$.

Equation (6) naturally gives rise to clusterization, i.e., time intervals characterized by an intense activity with a high rate of peaks (high λ), interspersed with quiescent periods, during which the rate drops significantly (low λ). The larger the α, the shallower the power-law regime at long WTs, and the more clustered the time profile (Aschwanden & McTiernan 2010; Aschwanden et al. 2014). The details of how clustered the time profile looks, in particular how the shot rate varies with time, are directly described by Equation (6). At a given average rate $\bar{\lambda}$, by increasing α the variance of λ increases correspondingly; that is, the shot rate varies more wildly. This means deviating more and more from the constant-rate case, thus enhancing the clustering character. Figure 1 illustrates the difference between a time-varying process like $(\alpha = 1, \beta = 0)$ in Equation (6) and a constant one sharing the same mean rate over a 100 s time window. The temporal sequence of events for the former is evidently more clustered than that of the latter and, in spite of the typical fluctuations of a Poisson point process, tracks the behavior of $\lambda(t)$. It is worth nothing that, in general, in a Poisson process individual events are independent of each other and, as such, have no memory of the events that occurred earlier, *regardless* of whether the expected rate λ is constant or time dependent. The difference instead lies in the observed average rates as a function of time, so not on (a) but on (b). Depending on whether $\lambda(t)$ varies either in a deterministic way or randomly with/without memory, the average rate inherits the corresponding degree of correlation.

The WTDs we wanted to model are characterized by rare long WTs, where the count statistics are so low that one cannot use a simple χ^2 minimization to fit the expected distribution of Equation (8) to the counts collected in each bin. However, merging the bins so as to have enough counts loses information and resolution. We therefore devised a log likelihood based on Poisson statistics, which is essentially the C statistic (Cash 1979) and holds exactly even in the low-count regime. We used it in the context of a Bayesian Markov chain Monte Carlo approach. The details are reported in Appendix.

3. RESULTS

Table 1 reports the best-fit parameters for all of the WTDs we considered. In all cases the model of Equation (8) provides an acceptable description. The lowest confidence level is that of BATSE (3.0%), still comparable with the nominal 5% usually adopted as a threshold. The BATSE sample is the largest (6,560 WTs), so the high statistical sensitivity is likely to enhance small deviations from the model.

Figure 2 displays the WTDs for the γ-ray peak samples only. Apart from the GBM, whose power-law index is significantly steeper, the BAT and BATSE samples are fit with comparable indices, $2.06^{+0.10}_{-0.09}$ and 1.76 ± 0.04, respectively. This is remarkable given the different kind of detectors, energy passbands, and different GRB populations each instrument is mostly sensitive to (Band 2006). The soft and hard BATSE samples have the same index, showing no significant dependence on the energy channel. We investigated the reasons for the steeper WTD of the GBM set as follows: the dearth of long WTs is likely due to the shorter scanned time intervals, mostly from −30 to 300 s (Section 2.1.3). We therefore truncated the light curves of the *Swift*/BAT set and revised the WT selection accordingly. The results are reported in Table 1 as the BATtrunc set, which includes 1,445 WTs. Compared with the original BAT set, the WTD of the truncated data becomes steeper, from $2.06^{+0.10}_{-0.09}$ to $2.22^{+0.16}_{-0.15}$, i.e., compatible with the GBM value within uncertainties. Hence, we interpret the slightly steeper value of the GBM set as the result of shorter time profiles that disfavor long WTs.

Figure 3 displays the BAT-X set (squares) with the corresponding best-fit model. The power-law index is $1.66^{+0.07}_{-0.06}$, i.e., compatible with BATSE sets within uncertainties. What is more, *merging X-ray flares did not change the stochastic nature exhibited by the WTD, but extended its dynamical range by at least one order of magnitude with WTs as long as* 10^5 *s. A common stochastic model is found to well describe the WTD observed across more than five orders of magnitude.*

A similar result is obtained when one restricts the sample to the known-redshift sample BAT-Xz in the GRB rest frame (circles in Figure 3): here the power-law index is $1.55^{+0.11}_{-0.10}$, i.e., somewhat shallower. The rest-frame characteristic time is significantly shorter because of cosmic dilation, 1.3 s instead of the observer-frame values of 6–7 s.

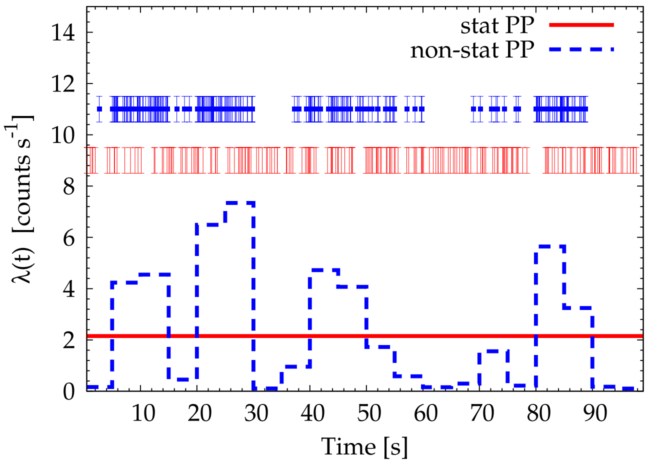

Figure 1. Example of time-varying Poisson process with variable rate $\lambda(t)$ (dashed) assuming $\alpha = 1$ and $\beta = 0$ in Equation (6) and a constant one (solid) with the same mean values. Squares and vertical bars in the top region mark the corresponding event times that were generated as a consequence. The pronounced clusterization of the variable case over the constant one is clear.

Table 1
Best-fit Parameters of the Model in Equation (8) Obtained for Different WTDs

Sample	Size	α	β (s)	PL Index (= 3 − α)	CL (%)
BAT	1582	$0.94^{+0.09}_{-0.10}$	$6.53^{+1.22}_{-0.98}$	$2.06^{+0.10}_{-0.09}$	26.4
BATSE	6560	1.24 ± 0.04	$1.53^{+0.19}_{-0.16}$	1.76 ± 0.04	3.0
BATSE12	5156	1.19 ± 0.05	$2.72^{+0.33}_{-0.29}$	1.81 ± 0.05	7.5
BATSE34	4912	1.18 ± 0.05	$1.23^{+0.18}_{-0.16}$	1.82 ± 0.05	76.6
GBM	1839	$0.64^{+0.16}_{-0.17}$	$6.76^{+1.44}_{-1.14}$	$2.36^{+0.17}_{-0.16}$	36.3
BATtrunc	1445	$0.78^{+0.15}_{-0.16}$	$6.99^{+1.63}_{-1.28}$	$2.22^{+0.16}_{-0.15}$	5.2
BAT-X	854	$1.34^{+0.06}_{-0.07}$	$6.33^{+1.54}_{-1.20}$	$1.66^{+0.07}_{-0.06}$	5.4
BAT-Xz	359	$1.45^{+0.10}_{-0.11}$	$1.26^{+0.72}_{-0.42}$	$1.55^{+0.11}_{-0.10}$	18.5

Note. Size is the number of WTs.

We also searched for possible correlations between WTs and peak intensities and between WTs and peak fluences of adjacent pulses, but we found none. Finally, we repeated the analysis for various subsets of GRBs by requiring a minimum number of peaks per GRB and found no significant difference.

3.1. γ-Ray Peaks versus X-Ray Flares

Figure 4 shows the distribution of the number of γ-ray peaks per GRB for two different classes of GRBs, depending on whether their subsequent X-ray emission contains X-ray flares. Surprisingly, it is found that almost all GRBs (23/25) with $N \geqslant 8$ γ-ray peaks have no X-ray flares, although the two groups have comparable size, 131 and 163 GRBs with and without flares, respectively. The two distributions are unlikely to share a common population of events: a Kolmogorov–Smirnov (KS) test yields a mere 0.21% probability, that is, they are different with 3.1σ (Gaussian) confidence. We visually inspected each of these γ- and X-ray light curves and found only one case of a flareless GRB, whose X-ray light curve exhibited some low-level flaring activity that did not pass the 90% confidence threshold in the flare sample selection (Section 2.1.4). Therefore, GRBs with many pulses are unlikely to exhibit flares in the subsequent declining X-ray emission.

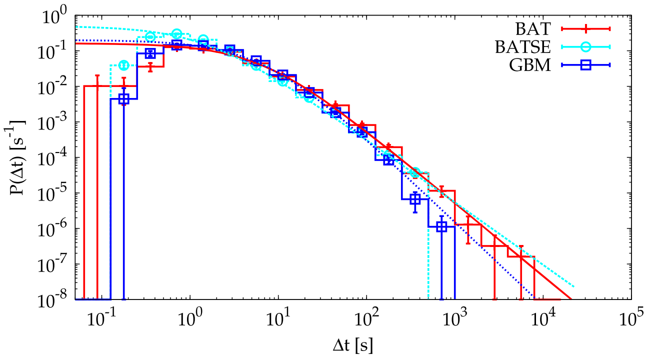

Figure 2. WTDs of γ-ray pulses of the BAT (crosses), BATSE (circles), and GBM (squares) samples with their corresponding best-fit models. Error bars are the (normalized) square root of counts and are just indicative.

4. DISCUSSION

Our results may be summarized in four fundamental aspects:

1. The γ-ray peaks and X-ray flares are compatible with being different aspects of the same stochastic process, which goes on after the end of the GRB itself and spans more than five orders of magnitude in time.
2. Short (interpulse) and long (quiescent) WTs between γ-ray peaks are different realizations of the same stochastic process, the latter being only less frequent than the former; hence, a GRB with QTs and another without are by no means more different from each other than any other kinds of GRBs are.
3. GRBs with several ($\geqslant$8) γ-ray pulses are unlikely to exhibit X-ray flares after the end of the prompt emission.
4. The γ-ray peaks and X-ray flares tend to cluster in much the same way that solar flares, energetic particle events, and CMEs do, even though the processes may be different.

The lognormal nature of the WTD originally claimed (Li & Fenimore 1996) has recently been shown to possibly be an artifact of the peak-detection algorithms in the short WT end ($\lesssim$1 s), where peaks significantly overlap and can hardly be separated (Baldeschi & Guidorzi 2015). We found that the long-value (greater than a few seconds) tail no longer needs to be described as the sum of a lognormal tail and a power-law excess due to the presence of QTs, which were interpreted as a different component (Nakar & Piran 2002; Quilligan et al. 2002; Drago & Pagliara 2007). This apparent diversity also concerns the so-called precursors (Lazzati 2005; Burlon et al. 2008, 2009; Charisi et al. 2014), which are nothing but emission periods that are less intense than the subsequent activity from which they are separated by a QT. Our results (1 and 2) show that all kinds of WTs, including precursors, can be described within a common stochastic process, and this holds all the way up to late X-ray flares, thus pointing toward a common mechanism, which keeps on working during and after the end of the prompt γ-ray emission, before the afterglow emission due to the interaction with the external medium takes over.

Another question concerns the break at low values in the WTD modeled in terms of the characteristic WT β: is it an intrinsic property or is it entirely due to the low efficiency at short values of the peak detection algorithm? The capability of separating overlapping structures depends on a number of variables, such as on the ratio between WT and peak widths, on intensities, and on temporal structures. Although the drop at

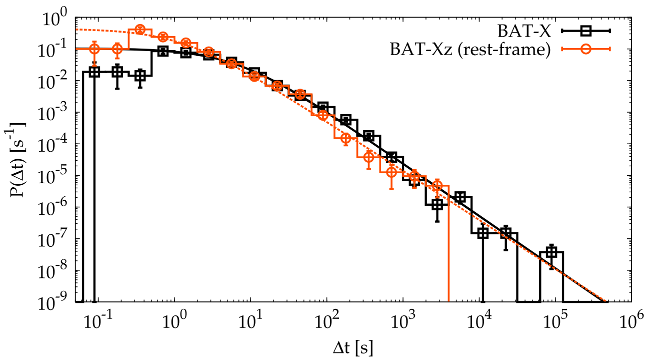

Figure 3. WTDs of γ-ray pulses and X-ray flares of BAT-X (squares) and of BAT-Xz (circles) sets with their corresponding best-fit models. Error bars are the (normalized) square root of counts and are just indicative.

$\Delta t \lesssim 0.5$ s is certainly due to the algorithm efficiency, the break itself modeled with β is more complex: β is shorter at harder energies (Table 1). A given pulse has a narrower temporal structure at harder energies (Fenimore et al. 1995), whereas in the softest energy channels there is a slow-varying component (Vetere et al. 2006). The presence of such a soft component might hinder the peak identification in some cases, so we examined the light curves in the harder channels. Visual inspection suggests that the paucity of subsecond WTs with respect to the power-law extrapolation is real and is unlikely to be a mere artifact of the peak identification process. In addition, minimum pulse widths observed in GRB profiles typically are in the range 0.1–1 s (Fenimore et al. 1995; Norris et al. 1996; Margutti et al. 2011). The MEPSA efficiency is above 10% for such pulse widths, for WTs >0.5 s, and for measured S/N >5 (Guidorzi 2015). It is therefore unlikely that the algorithm efficiency is entirely responsible for the observed exponential cutoff observed in the low end of the WTDs.

4.1. A Simple Toy Model

We devised a very simple toy model to explore more in detail how a time-dependent Poisson process like the one of Equation (6) could be obtained in a GRB engine. For the sake of clarity, suppose each pulse marks the accretion of a single fragment of a hyperaccreting disk. Actually, the idea behind this model is more general and only deals with the sequence of bursty emission episodes and their probability of occurring within a given time. However, hereafter we refer to the model of a hyperaccreting disk being fragmented as the source of the stochastic process that is responsible for the prompt γ-ray emission (Woosley 1993; MacFadyen & Woosley 1999) as well as for the subsequent X-ray flare activity (King et al. 2005; Perna et al. 2006; Kumar et al. 2008; Cannizzo & Gehrels 2009; Geng et al. 2013). We briefly summarize the basic ingredients of the model, which are then thoroughly described in the remaining part of this section:

1. A number of fragments are independently accreted with the same, constant, probability per unit time.
2. The number of available fragments is obviously decreasing with time; this naturally leads to a time-dependent Poisson process whose mean accretion rate decreases with time.
3. At the beginning, if the mean rate is too high ($\lambda > 1/\beta$), accretion becomes inefficient and is suppressed by a factor of $\exp(-\lambda\beta)$.
4. For some (~30%) GRBs, the reservoir of fragments is split into two separate groups sharing the same individual accretion probability per unit time, but with the second group becoming available only at later times (e.g., the late group could be identified with the outer part of the accretion disk).

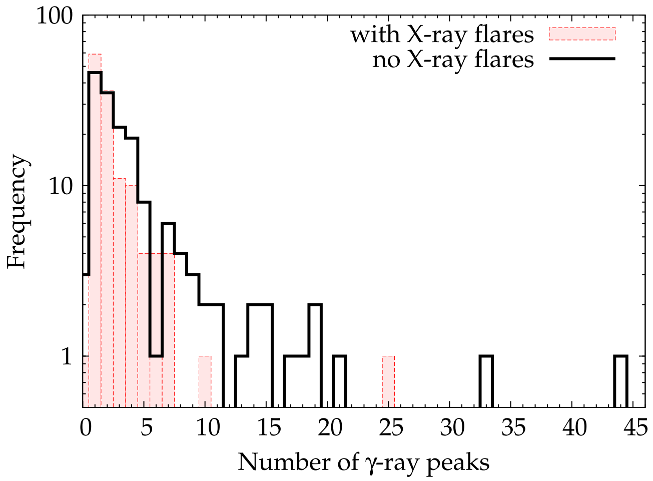

Figure 4. Distribution of number of γ-ray peaks per GRB for two distinct subsets of the *Swift* BAT-X sample, depending on the presence or lack of flares in the subsequent X-ray emission. Almost all (23/25) GRBs with at least eight γ-ray peaks have no X-ray flares. A KS test yields a common population probability of 0.21%.

Let us assume that the disk or the inner part of it has been split into a number of fragments, each of which has the same given probability of accreting per unit time, independently of the others. The probability for a given fragment to survive up to a given time t is proportional to $\exp(-t/\tau)$, where τ is the mean accretion time for each fragment. The total expected rate scales as the number of fragments that are still available, $\lambda = |\dot{N}(t)| = (N_0/\tau)\exp(-t/\tau) = N(t)/\tau$. The analogous $f(\lambda)$ to Equation (6) is found as

$$f(\lambda)d\lambda \propto |dt| = \tau\frac{d\lambda}{\lambda}, \tag{9}$$

which corresponds to the $\alpha = 1$ case in Equation (6) at $\lambda \ll 1/\beta$. Rather than a continuous varying, $\lambda(t)$ of this model is described more exactly by a piecewise Poisson process like the one of Equations (2)–(3), where $\lambda_i = i/\tau$ is the expected rate when i fragments are left over. All terms have equal-weight ϕ_is because each piecewise constant process contributes one WT. The resulting WTD is thus given by Equation (2):

$$P(\Delta t) = \frac{1}{N_0}\sum_{i=1}^{N_0}\frac{i}{\tau}\, e^{-i\,\Delta t/\tau}, \tag{10}$$

which can also be expressed as

$$P(x) = \frac{x\left[N_0\, x^{N_0+1} - \left(N_0+1\right)x^{N_0} + 1\right]}{N_0\tau(1-x)^2}, \tag{11}$$

where $x = e^{-\Delta t/\tau}$. In Figure 5 an example of such a WTD is shown, with $N_0 = 20$ initial fragments, $\tau = 1$ s. As time goes by, $\lambda(t)$ decreases and the e-folding of the individual exponential WTDs (thin solid) increase correspondingly. As a result, the total WTD (thick solid) shows a power-law regime with index two at intermediate values of Δt. At $\Delta t \lesssim \tau/N_0$ the

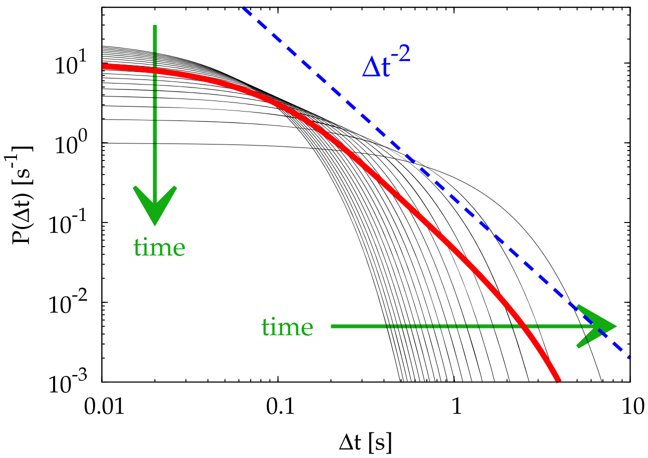

Figure 5. Series of exponential WTDs (thin solid) of a sequence of **constant** Poisson processes with progressively increasing e-folding. At intermediate values the mean WTD (thick solid) scales as a power law with index two, shown for comparison (dashed).

total WTD is dominated by the initial exponential with e-folding τ/N_0, when fragments are all available. This agrees with the result that the intrinsic (i.e., corrected for the algorithm efficiency) WTD at short values is likely exponential, that is, compatible with a constant Poisson process (Baldeschi & Guidorzi 2015).

Thus far, with reference to Equation (6), our model implicitly assumed $\beta = 0$ (see Equation (9)). However, our attempt to reproduce the observed WTD with the piecewise constant process of Equation (10) failed to model the observed break at $\Delta t \sim 1/\beta$. So we required that, when the expected rate becomes comparable or higher than $1/\beta$, the number of observed WTs is suppressed by a factor of $\exp(-\lambda\beta)$ with respect to our model. This can be interpreted as if, when the number N of fragments that can be readily accreted is such that the expected rate is $\lambda = N/\tau \gtrsim 1/\beta$, the overall process becomes inefficient and the rate is suppressed by $\exp(-\lambda\beta)$. In other words, the number of WTs shorter than β is smaller than what is expected from Equation (9). This introduces some degree of memory in the initial stages of the accretion process: as long as the number of fragments ready to be accreted is too high ($\tau/N \lesssim \beta$), some of them are temporarily halted from accreting by some mechanism connected with the accretion rate itself. For instance, this self-regulating mechanism could be driven by the magnetic field (e.g., Proga & Zhang 2006; Uzdensky & MacFadyen 2006; Bernardini et al. 2013), which is known to have a complex role in accretion processes of utterly different objects such as T Tauri stars (Stephens et al. 2014). However, we cannot provide a more specific and physical justification for the exponential character of this self-quenching mechanism, which is therefore ad hoc in its present formulation.

We assumed the logarithmic average and 1σ scatter of the BAT-X WTD, 16.8 s and a multiplicative scatter of 7.1, to generate the values for τ for each simulated burst. The number of generated peaks in each simulated curve was taken from the observed distribution and was augmented by 20% to ensure that the detected peaks were enough (because some are missed by the algorithm). The peak times for each simulated curve were randomly generated from an exponential distribution with e-folding τ, i.e., independently from each other. To mimic the drop in the peak detection efficiency at short WTs as well as the mechanism mentioned above about the suppression at high rates, we overlooked each peak occurring within 0.5 s of the previous one, and through a binomial we assigned each Δt a probability $\exp(-\beta/\Delta t)$ of being observed, where β was set to the fitted value of the real WTD (Table 1).

To obtain a good match with the observed WTD over the same range, we had to make a further assumption: we assumed that for a fraction of GRBs (~30%) randomly selected through a binomial, the disk is fragmented equally in two groups, the first of which is available for being accreted from the beginning ($t_0 = 0$), and the second one becomes available from $t_0 = 50\,\tau$ on, where τ is the common mean accretion time for each individual fragment from $t = t_0$. The reason behind this is the observation of two similar bunches of γ-ray peaks interspersed with a long QT (up to several tens of seconds) for a small fraction of GRBs. Physically, this could be the result of an outer part of the disk being accreted at later times with respect to the inner one or, more in general, a delayed additional energy reservoir becoming available for late internal dissipation, with a minimum variability timescale comparable with that of the early prompt emission (Fan & Wei 2005; Lazzati & Perna 2007; Troja et al. 2014). While the choice of the fraction of such GRBs and the duration of the quiescence period are somewhat arbitrary, the good match between simulated and real WTD does not depend crucially on them. Overall, the goal here is just to show the plausibility of the essential properties of this model, which can reproduce the observed properties in spite of the simple assumptions. We ended up with a set of 903 simulated WTs, whose distribution is compared with the real one in Figure 6.

We further tested the consequences of this toy model by studying the distribution of the ratio between adjacent WTs. Whereas WTDs describe how WTs distribute as a whole, losing information on their temporal sequence, the ratio distribution focuses on that. We therefore selected from the BAT-X as well as from the simulated sample the GRBs with $\geqslant$3 peaks, so as to have at least two WTs, and derived the two distributions shown in Figure 7. A KS test between the two sets yields 43% probability that they were drawn from a common population. The logarithmic mean and dispersion for the real (simulated) data are $\mu = 0.14$ and $\sigma = 0.72$ ($\mu = 0.09$ and $\sigma = 0.81$). Similar results are obtained by adopting other nonparametric tests, such as the Wilcoxon–Mann–Whitney or the more sensitive Epps–Singleton one (Epps & Singleton 1986), respectively yielding 45% and 9% probability. Interestingly, simply replacing Equation (9) with a constant Poisson process and applying the very same subsequent steps, one ends up with a narrower and more zero-centered logarithmic ratio distribution, $\mu = 0.013$ and $\sigma = 0.32$, which is rejected with high confidence (p value $<2 \times 10^{-16}$) from a KS test. This means that for a constant process the ratio is, on average, closer to one, and is less scattered around it than real data. The compatibility of the ratio distribution predicted by the toy model with the real one proves that the temporal sequence of WTs is compatible with an evolving Poisson process and is incompatible with a constant one on long timescales. In particular, X-ray flares are nothing but some of the last fragments that are left over and that are accreted on long timescales, when the rate decreases in a granular way, following the very same stochastic process ruling the accretion of the earliest ones. Hence, no correlation is to be expected between γ-ray prompt emission duration (T_{90}) and X-ray flare times, in agreement with observations (Liang et al. 2006).

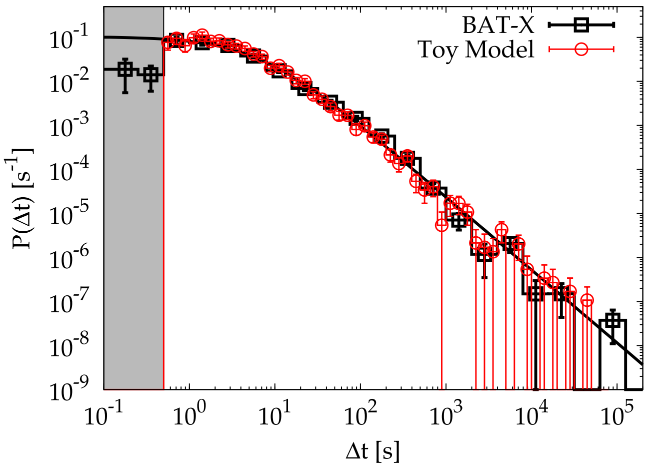

Figure 6. WTD for the *Swift* BAT-X sample (squares) compared with a simulated sample of 903 WTs derived from a toy model (circles). The shaded interval is where the peak search algorithm efficiency drops.

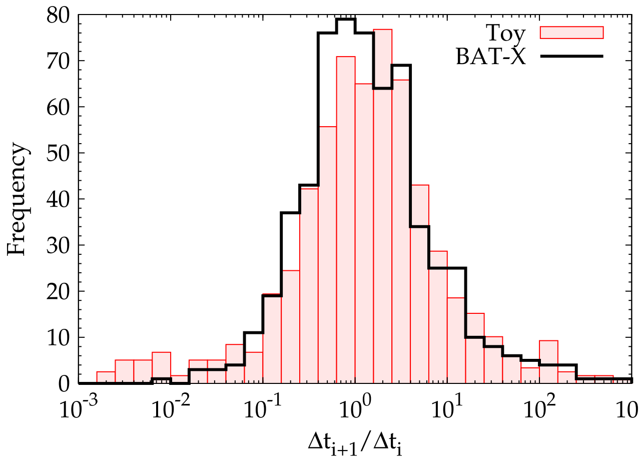

Figure 7. Distribution of the ratio of adjacent WTs of the *Swift* BAT-X sample (solid) and of the toy-model sample (shaded).

Finally, the result of Section 3.1 can be easily explained: GRBs with many γ-ray peaks accrete fragments rapidly with relatively short τ, so that at late time very few or none at all are left over for X-ray flares. The same result could be explained differently though: multipeaked GRBs could have on average a brighter early X-ray afterglow continuum that outshines possible X-ray flares, which would then go unseen.

Overall, we assumed a direct connection between the emission and observed times of the peaks. Within the context of internal shocks, the observed time profiles of both prompt γ-rays and late X-ray flares are strictly connected to the emission history (Kobayashi et al. 1997; Maxham & Zhang 2009). Should this not be the case, little could be inferred about emission times—and potentially the times of individual accretion episodes—from the study of the observed WTD. However, this connection becomes more complex due to the variety of Lorentz factors associated with the wind of shells colliding with each other. Even though the intrinsic duration of the GRB engine activity may differ by a factor of a few from the observed one (Gao & Mészáros 2014), on average the temporal sequence of mutual collisions between randomly assigned Lorentz-factor shells should track the emission time history. The nature of a given WTD is not altered as a whole when one passes from the emission to the observed times. In fact, each shell has a Lorentz factor—which in principle can make the observed WTs very different from the emitted ones—that is independent of the WTs preceding and following that shell. This statistical independence ensures that the observed WTD keeps memory on the emission time distribution. Only at late times, when the average Lorentz factor is expected to systematically decrease and the statistically independent character likely begins to fail, long WTs are likely to be affected as a consequence.

4.2. Solar Activity: Analogies and Differences

It is remarkable and intriguing that WTDs of both solar eruptive events (X-ray flares, radio storms, high-energy particle events, CMEs) and of GRBs can be modeled with the same kind of time-dependent Poisson process. The power-law characterization of the WTD heavy tail must not be overinterpreted from a mathematical viewpoint because power laws are, in general, what one ends up with when dealing with the sum of independent heavy-tailed variables. It works much in the same way that a normal distribution is the final outcome of the sum of independent finite-variance variables. In addition, claiming that data are power-law distributed is contrived whenever the explored range does not cover at least two decades (Stumpf & Porter 2012). In this sense, invoking an SOC-driven mechanism for GRBs purely based on the power-law character of the WTD, and possibly of the energy distribution too, as suggested for X-ray flares from GRBs (Wang & Dai 2013) or from other black hole systems (Wang et al. 2014), is a stretched interpretation of the data, as we explain below.

The same or very similar power-law indices imply that both processes have very similar degrees of clusterization, with analogous swings between intense and low-activity periods, apart from temporal rescaling (seconds for GRBs, hours for the Sun). However, one has to be careful about extending this analogy to a common physical mechanism. Overall, there is a fundamental difference in terms of dynamical systems between GRB inner engines during core collapse and the Sun: for the latter, the regions where eruptive phenomena take place continuously receive energy, which is then released through avalanches, thus making the SOC interpretation plausible (although alternatives based on MHD turbulence seem equally compatible with observations). Instead, GRB engines are systems that start with a configuration that is very far from equilibrium and evolve very fast, using up all of the available energy, which—no matter how much—is *limited*. A GRB inner engine cannot return to its original configuration; it goes through an obviously *irreversible* evolution, whereas this is not the case for the solar active regions over sufficiently long timescales. For this reason, one need not invoke SOC mechanisms related to accretion disks; in particular, there is no need for a mechanism like the one proposed to explain $1/f$ fluctuations in black hole power spectra (Mineshige et al. 1994).

Therefore, a simple time-varying Poisson process explains the secular evolution of the mean rate of bursts or flares as well as the stochastic, independent character of individual energy-release episodes. This model disregards the physical origin of fragmentation and how energy is distributed among different fragments. Thus, in principle, it is compatible with various physical drivers, such as gravitational (Perna et al. 2006) or magnetorotational instability (Proga & Zhang 2006).

5. CONCLUSIONS

In this paper we studied the WTDs of GRB γ-ray pulses in three catalogs: *CGRO*/BATSE, *Fermi*/GBM, and *Swift*/BAT. For the latter, for the first time we merged γ-ray pulses and X-ray flares detected with *Swift*/XRT belonging to the same GRBs, and for a subsample the same analysis was carried out in the source rest frame. We found that all WTDs can be described in terms of a common time-varying Poisson process that rules different waiting-time intervals, which thus far in the literature have been treated differently. Specifically, we showed that short WTs ($\lesssim$1 s), long QTs ($\gtrsim$10 s), all the way up to late-time X-ray flares are the manifestation of a common stochastic process. GRB WTDs exhibit heavy tails that are modeled with power laws over four to five decades in time with indices in the range 1.7–2.1, depending on the relative weight of late-time events, such as X-ray flares, in each GRB sample. Because of the ubiquitous nature of power laws (a central limit theorem for heavy-tailed distributions), the character of WTDs must not be imbued with a mystical sense or overinterpreted as evidence for a universal process. In this sense, the similarity of the WTD power-law index with that of solar eruptive phenomena, such as flares and CMEs, proves nothing but a similar degree of clusterization in time. Nonetheless, it is remarkable that the WTDs of γ-ray pulses and that of X-ray flares not only have compatible power-law indices but they join and extend the dynamical range for a common sample of GRBs. All this points to a common stochastic process ruling both phenomena. The unification under a common process of all different kinds of WTs in GRBs (short interpulse times, long QTs, time intervals following precursors, time intervals between the end of the γ-ray prompt emission and subsequent X-ray flares) is a new result.

Another noteworthy result is that GRBs with many ($\geqslant$8) γ-ray pulses are unlikely (3.1σ confidence in Gaussian units) to exhibit X-ray flares in their subsequent early X-ray emission. This result is naturally explained in the context of the time-varying Poisson process: many pulses observed in the prompt of a given GRB are indicative of a relatively short mean accretion time for a single disk fragment. Consequently, most of the available fragments are consumed during the prompt phase, with very few or none at all left over for the subsequent phase.

In light of the irreversible evolution of GRB inner engines, the interpretation of a time-varying Poisson process appears to be simple and reasonable: the secular evolution of the expected rate of events is naturally linked to the energy reservoir being gradually used up, whereas the stochastically independent accretion of individual fragments is explained by the Poissonian character of the process.

Although self-organized criticality models naturally predict power-law-tailed distributions of WTs and energy, drawing upon this kind of dynamics for GRBs might be premature. Other equally plausible alternatives, such as fully developed MHD turbulence, can explain the same properties, as was suggested for the solar case. Possible evidence for turbulence in GRBs has also been suggested from the analysis of power density spectra (Beloborodov et al. 1998, 2000; Guidorzi et al. 2012; Dichiara et al. 2013). Yet, we find that a simple time-varying Poisson process such as that of a system gradually using up all the available pieces already provides a remarkably accurate description.

The energy distribution, which was beyond the scope of this paper, will help to further constrain the stochastic process and possibly clarify whether more complex dynamical models, such as SOC or MHD turbulence, are to be considered.

We are grateful to the anonymous referee for a constructive and insightful review. The PRIN MIUR project on “Gamma-ray bursts: From progenitors to physics of the prompt emission process,” P.I. F. Frontera (Prot. 2009 ERC3HT), is acknowledged.

APPENDIX
LOG LIKELIHOOD TO FIT THE DISTRIBUTIONS

Let the WTD consist of N logarithmically spaced bins, each collecting C_i counts. Let $\Delta t_{i,1}$ and $\Delta t_{i,2}$ be the lower and upper bounds of the ith bin ($i = 1, \ldots, N$). Integrating Equation (8) within this time interval yields the corresponding expected counts, $E_i(\alpha,\beta)$, where we explicitly meant that it depends on the model parameters:

$$\begin{aligned} E_i(\alpha,\beta) &= C_{\rm tot} \int_{\Delta t_{i,1}}^{\Delta t_{i,2}} P(\Delta t)\, d(\Delta t) \\ &= C_{\rm tot}\, \beta^{2-\alpha} \Big[\left(\beta + \Delta t_{i,1}\right)^{\alpha-2} \\ &\quad - \left(\beta + \Delta t_{i,2}\right)^{\alpha-2} \Big] \end{aligned} \tag{A.1}$$

where $C_{\rm tot} = \sum_{i=1}^{N} C_i$, and β is a function of both model parameters (Section 2.2). The probability of C_i counts is ruled by the Poisson distribution where E_i is the expected value:

$$P\left(C_i \middle| \alpha, \beta\right) = e^{-E_i} \frac{E_i^{C_i}}{C_i\,!}, \tag{A.2}$$

where the dependence on model parameters is implicit through E_i. The total probability is thus

$$P(C|\alpha,\beta) = \prod_{i=1}^{N} e^{-E_i} \frac{E_i^{C_i}}{C_i\,!}, \tag{A.3}$$

where C is the set of observed counts per bin $\{C_i\}$ ($i = 1, \ldots, N$). The corresponding negative log likelihood is therefore

$$\begin{aligned} L(\alpha,\beta) &= -\sum_{i=1}^{N} \log\left(P\left(C_i \middle| \alpha,\beta\right)\right) \\ &= \sum_{i=1}^{N} \left(E_i + \log\left(C_i\,!\right) - C_i \log E_i\right). \end{aligned} \tag{A.4}$$

We determine the best-fit model parameters and their uncertainties in the Bayesian context. The posterior PDF of the parameters for a given observed distribution C is (Bayes theorem)

$$P(\alpha,\beta|C) = \frac{P(C|\alpha,\beta)\, P(\alpha,\beta)}{P(C)}, \tag{A.5}$$

where the first term in the numerator of the right-hand side of Equation (A.5) is the likelihood function of Equation (A.3), $P(\alpha,\beta)$ is the prior distribution of the model parameters, and the denominator is the normalization term. We assumed a uniform prior distribution because no a priori information is available on the model parameters. The mode of the posterior probability of Equation (A.5) is therefore found by minimizing Equation (A.4).

We estimate the posterior density of the model parameters through a Markov chain Monte Carlo (MCMC) algorithm, such as the random-walk Metropolis–Hastings in the implementation of the R[9] package MHadaptive[10] (v.1.1-8). We initially approximate the posterior using a bivariate normal distribution centered on the mode and with a covariance matrix obtained by minimizing Equation (A.4). For each WTD we generate 5.1×10^4 sets of simulated model parameters and retain one of every five MCMC iterations after excluding the first 1,000. The remaining 10^4 sets of parameters are therefore used to approximate the posterior density. Finally, once the best-fit model parameters are determined, the bivariate posterior distribution of (α, β) is sampled via MCMC simulations, which yield the expected value and 90% confidence intervals for each of them.

As a matter of fact, because the bins in the low end of the distribution are strongly affected by the poor efficiency of mepsa, these are to be ignored. In practice, one has to replace in Equation (A.1) $C_{\rm tot}$ with $C'_{\rm tot} = \sum_{i=k_1}^{k_2} C_i$, where k_1 and k_2 are the first and last bins to be considered. In addition, the same E_i in Equation (A.1) has to be further divided by a renormalizing factor so that it becomes

$$E_i(\alpha, \beta) = C'_{\rm tot}\frac{\left(\beta + \Delta t_{i,1}\right)^{\alpha-2} - \left(\beta + \Delta t_{i,2}\right)^{\alpha-2}}{\left(\beta + \Delta t_{k_1,1}\right)^{\alpha-2} - \left(\beta + \Delta t_{k_2,2}\right)^{\alpha-2}}. \quad \text{(A.6)}$$

For the WTDs discussed in the present paper, we considered $\Delta t \geqslant 0.5$ s ($\Delta t \geqslant 0.2$ s) in the observer (source) rest frame.

To assess the goodness of the fit for a given WTD, we use each set of simulated values for (α, β) to generate as many synthetic WTDs from the posterior predictive distribution. Hence, for a given observed WTD, we directly calculate 10^4 synthetic realizations of the same WTD. For each of these WTDs, we calculate the negative log likelihood with Equation (A.4) and derive a corresponding distribution of values, against which the value obtained from the real WTD is checked. This comparison directly provides a confidence level of modeling the observed WTD in terms of the best-fit model of Equation (8).

REFERENCES

Arzner, K., & Güdel, M. 2004, ApJ, 602, 363
Aschwanden, M. J., Crosby, N. B., Dimitropoulou, M., et al. 2014, SSRv
Aschwanden, M. J., & McTiernan, J. M. 2010, ApJ, 717, 683
Baldeschi, A., & Guidorzi, C. 2015, A&A, 573, L7
Band, D. L. 2006, ApJ, 644, 378
Beloborodov, A. M., Stern, B. E., & Svensson, R. 1998, ApJL, 508, L25
Beloborodov, A. M., Stern, B. E., & Svensson, R. 2000, ApJ, 535, 158
Bernardini, M. G., Campana, S., Ghisellini, G., et al. 2013, ApJ, 775, 67
Bernardini, M. G., Margutti, R., Chincarini, G., Guidorzi, C., & Mao, J. 2011, A&A, 526, A27
Boffetta, G., Carbone, V., Giuliani, P., Veltri, P., & Vulpiani, A. 1999, PhRvL, 83, 4662
Burlon, D., Ghirlanda, G., Ghisellini, G., Greiner, J., & Celotti, A. 2009, A&A, 505, 569
Burlon, D., Ghirlanda, G., Ghisellini, G., et al. 2008, ApJ, 685, L19
Burrows, D. N., Romano, P., Falcone, A., et al. 2005, Sci, 309, 1833
Cannizzo, J. K., & Gehrels, N. 2009, ApJ, 700, 1047
Cash, W. 1979, ApJ, 228, 939
Charisi, M., Márka, S., & Bartos, I. 2014, in press, arXiv:1409.2491
Chincarini, G., Mao, J., Margutti, R., et al. 2010, MNRAS, 406, 2113
Chincarini, G., Moretti, A., Romano, P., et al. 2007, ApJ, 671, 1903
Cox, D. R., & Isham, V. 1980, in Point Processes (London: Chapman & Hall)
Curran, P. A., Starling, R. L. C., O'Brien, P. T., et al. 2008, A&A, 487, 533
Dichiara, S., Guidorzi, C., Amati, L., & Frontera, F. 2013, MNRAS, 431, 3608
Drago, A., & Pagliara, G. 2007, ApJ, 665, 1227
Drago, A., Pagliara, G., & Schaffner-Bielich, J. 2008, JPhG, 35, 014052
Eastwood, J. P., Wheatland, M. S., Hudson, H. S., et al. 2010, ApJL, 708, L95
Eckmann, J.-P., Moses, E., & Sergi, D. 2004, PNAS, 101, 14333
Epps, T. W., & Singleton, K. J. 1986, J. Stat. Comput. Simul., 26, 177
Evans, P. A., Willingale, R., Osborne, J. P., et al. 2014, MNRAS, 444, 250
Falcone, A. D., Morris, D., Racusin, J., et al. 2007, ApJ, 671, 1921
Fan, Y. Z., & Wei, D. M. 2005, MNRAS, 364, L42
Fenimore, E. E., in't Zand, J. J. M., Norris, J. P., Bonnell, J. T., & Nemiroff, R. J. 1995, ApJL, 448, L101
Fitzpatrick, G., McBreen, S., Connaughton, V., & Briggs, M. 2012, in Proc. SPIE, 8443, 8443B
Gao, H., & Mészáros, P. 2014, submitted arXiv:1411.2650,
Gavriil, F. P., Kaspi, V. M., & Woods, P. M. 2004, ApJ, 607, 959
Geng, J. J., Wu, X. F., Huang, Y. F., & Yu, Y. B. 2013, ApJ, 779, 28
Göğüş, E., Woods, P. M., Kouveliotou, C., et al. 1999, ApJL, 526, L93
Göğüş, E., Woods, P. M., Kouveliotou, C., et al. 2000, ApJL, 532, L121
Gruber, D., Goldstein, A., Weller von Ahlefeld, W., et al. 2014, ApJS, 211, 12
Gruber, D., Kruehler, T., Foley, S., et al. 2011, A&A, 528, A15
Guidorzi, C. 2005, MNRAS, 364, 163
Guidorzi, C. 2014, MEPSA: Multiple Excess Peak Search Algorithm, ascl:1410.002
Guidorzi, C. 2015, A&C, 10, 54
Guidorzi, C., Margutti, R., Amati, L., et al. 2012, MNRAS, 422, 1785
Hjorth, J., & Bloom, J. S. 2012, in Gamma-Ray Bursts, ed. C. Kouveliotou, R. A. M. J. Wijers, & S. Woosley (Cambridge: Cambridge Univ. Press), 169
Karsai, M., Kaski, K., Barabási, A.-L., & Kertész, J. 2012, NatSR, 2, 397
King, A., O'Brien, P. T., Goad, M. R., et al. 2005, ApJL, 630, L113
Kobayashi, S., Piran, T., & Sari, R. 1997, ApJ, 490, 92
Kumar, P., Narayan, R., & Johnson, J. L. 2008, MNRAS, 388, 1729
Lazzati, D. 2005, MNRAS, 357, 722
Lazzati, D., & Perna, R. 2007, MNRAS, 375, L46
Lepreti, F., Carbone, V., Giuliani, P., Sorriso-Valvo, L., & Veltri, P. 2004, P&SS, 52, 957
Li, C., Zhong, S. J., Wang, L., Su, W., & Fang, C. 2014, ApJL, 792, L26
Li, H., & Fenimore, E. E. 1996, ApJ, 469, L115
Liang, E. W., Zhang, B., O'Brien, P. T., et al. 2006, ApJ, 646, 351
MacFadyen, A. I., & Woosley, S. E. 1999, ApJ, 524, 262
Margutti, R., Guidorzi, C., & Chincarini, G. 2011, IJMPD, 20, 1969
Margutti, R., Guidorzi, C., Chincarini, G., et al. 2010, MNRAS, 406, 2149
Maxham, A., & Zhang, B. 2009, ApJ, 707, 1623
Meegan, C., Lichti, G., Bhat, P. N., et al. 2009, ApJ, 702, 791
Mineshige, S., Ouchi, N. B., & Nishimori, H. 1994, PASJ, 46, 97
Nakar, E., & Piran, T. 2002, MNRAS, 331, 40
Norris, J. P., Nemiroff, R. J., Bonnell, J. T., et al. 1996, ApJ, 459, 393
Oliveira, J. G., & Barabási, A.-L. 2005, Natur, 437, 1251
Paciesas, W. S., Meegan, C. A., Pendleton, G. N., et al. 1999, ApJS, 122, 465
Paciesas, W. S., Meegan, C. A., von Kienlin, A., et al. 2012, ApJS, 199, 18
Perna, R., Armitage, P. J., & Zhang, B. 2006, ApJL, 636, L29
Picoli, S., Castillo-Mussot, M. D., Ribeiro, H. V., et al. 2014, NatSR, 4, 4773
Platt, N., Spiegel, E. A., & Tresser, C. 1993, PhRvL, 70, 279
Popham, R., Woosley, S. E., & Fryer, C. 1999, ApJ, 518, 356
Proga, D., & Zhang, B. 2006, MNRAS, 370, L61
Quilligan, F., McBreen, B., Hanlon, L., et al. 2002, A&A, 385, 377
Ramirez-Ruiz, E., & Merloni, A. 2001, MNRAS, 320, L25
Ramirez-Ruiz, E., Merloni, A., & Rees, M. J. 2001, MNRAS, 324, 1147
Sakamoto, T., Barthelmy, S. D., Baumgartner, W. H., et al. 2011, ApJS, 195, 2
Stephens, I. W., Looney, L. W., Kwon, W., et al. 2014, Natur, 514, 597
Stumpf, M. P. H., & Porter, M. A. 2012, Sci, 335, 665
Swenson, C. A., & Roming, P. W. A. 2014, ApJ, 788, 30
Swenson, C. A., Roming, P. W. A., de Pasquale, M., & Oates, S. R. 2013, ApJ, 774, 2
Troja, E., Piro, L., Vasileiou, V., et al. 2014, in press, arXiv:1411.1415
Utsu, T. 1961, Geophys. Mag., 30, 521

---

[9] http://cran.r-project.org/

[10] http://cran.r-project.org/web/packages/MHadaptive/index.html

Uzdensky, D. A., & MacFadyen, A. I. 2006, ApJ, 647, 1192
Vetere, L., Massaro, E., Costa, E., Soffitta, P., & Ventura, G. 2006, A&A, 447, 499
Virgili, F. J., Mundell, C. G., Palshin, V., et al. 2013, ApJ, 778, 54
Wang, F. Y., & Dai, Z. G. 2013, NatPh, 9, 465
Wang, F. Y., Dai, Z. G., Yi, S. X., & Xi, S. Q. 2015, ApJS, 216, 8
Wheatland, M. S. 2000, ApJL, 536, L109
Wheatland, M. S. 2003, SoPh, 214, 361
Woosley, S. E. 1993, ApJ, 405, 273
Woosley, S. E., & Bloom, J. S. 2006, ARA&A, 44, 507